

Hydrogen Bonding Affects the [NiFe] Active Site of *Desulfovibrio vulgaris* Miyazaki F Hydrogenase: A Hyperfine Sublevel Correlation Spectroscopy and Density Functional Theory Study

Aruna Goenka Agrawal, Maurice van Gastel, Wolfgang Gärtner, and Wolfgang Lubitz*

Max-Planck-Institut für Bioanorganische Chemie, Stiftstrasse 34-36, D-45470 Mülheim an der Ruhr, Germany

Received: December 19, 2005; In Final Form: February 27, 2006

Pulse electron paramagnetic resonance and hyperfine sublevel correlation spectroscopy have been used to investigate nitrogen coordination of the active site of [NiFe] hydrogenase of *Desulfovibrio vulgaris* Miyazaki F in its oxidized “ready” state. The obtained ^{14}N hyperfine ($A = [+1.32, +1.32, +2.07]$ MHz) and nuclear quadrupole ($e^2qQ/h = -1.9$ MHz, $\eta = 0.37$) coupling constants were assigned to the N_ϵ of a highly conserved histidine (His88) by studying a hydrogenase preparation in which the histidines were ^{15}N labeled. The histidine is hydrogen-bonded via its $\text{N}_\epsilon\text{—H}$ to the nickel-coordinating sulfur of a cysteine (Cys549) that carries an appreciable amount of spin density. Through the hydrogen bond a small fraction of the spin density ($\sim 1\%$) is delocalized onto the histidine ring giving rise to an isotropic ^{14}N hyperfine coupling constant of about 1.6 MHz. These conclusions are supported by density functional calculations. The measured ^{14}N quadrupole coupling constants are related to the polarization of the $\text{N}_\epsilon\text{—H}$ bond, and the respective hydrogen bond can be classified as being weak.

Introduction

Hydrogenases catalyze the reversible oxidation of molecular hydrogen. Several classes of hydrogenases have been identified;¹ among these, the [NiFe] hydrogenases represent the largest class. These enzymes consist of two main subunits. The large subunit contains the active [NiFe] center, and the small subunit harbors one [3Fe4S] and two [4Fe4S] clusters that are involved in electron transport. The [NiFe] hydrogenase from *Desulfovibrio vulgaris* Miyazaki F has been crystallized, and the X-ray structure reveals that the nickel atom is ligated by the sulfurs of four cysteines, two in a terminal position and the other two in a bridging position between nickel and iron.^{2,3} Furthermore the iron atom carries three diatomic inorganic ligands, which have recently been confirmed by Fourier transform infrared (FTIR) spectroscopy to be two CN^- and one CO ligand.^{4,5} In the oxidized state, additional electron density is found between Ni and Fe,² which is absent in the structure of the reduced enzyme.³ A schematic overview of the active site in the oxidized state is shown in Figure 1a.

The [NiFe] site passes through several redox states in the enzymatic cycle. A characterization of the redox states has been performed by FTIR spectroscopy, using the shift of the vibrational frequencies of the CN^- and CO ligands attached to the Fe.^{4,6–8} In the most oxidized form, two paramagnetic redox states coexist, called Ni-A and Ni-B. The Ni-A state is characterized by g tensor components of 2.32, 2.24, and 2.01 and can be activated with molecular hydrogen only after hours. Ni-B has g tensor components of 2.33, 2.16, and 2.01 and is activated within minutes.^{9–11} After a one-electron reduction from Ni-A or Ni-B, the enzyme becomes electron paramagnetic resonance (EPR)-silent, and the states are named Ni-SU and Ni-SI₇, respectively. In the next step a conformational change

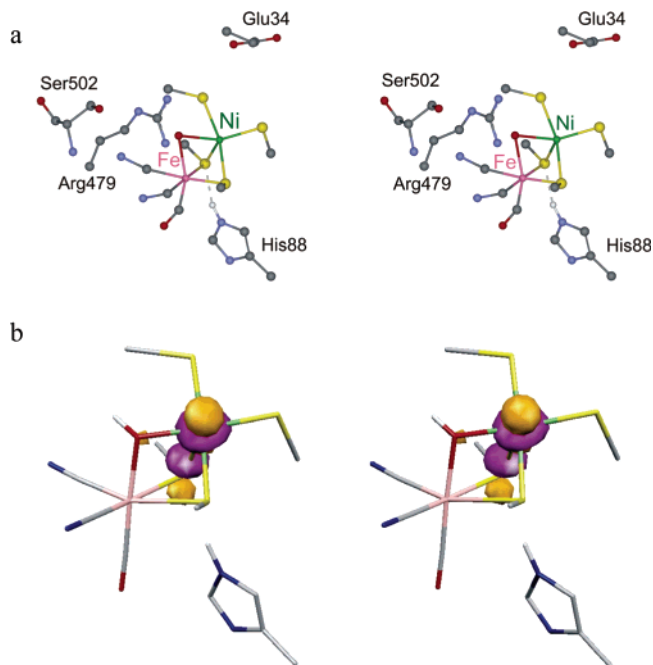


Figure 1. (a) Stereoview of the [NiFe] active site of *D. vulgaris* Miyazaki F hydrogenase, including the neighboring amino acids Arg479 (positively charged), Glu34 (protonated), Ser502, and His88 (hydrogen-bonded). The bridging ligand is an oxygen species in the oxidized state (modeled here as an OH^-). In the reduced state, a hydride has been detected in the bridging position.^{18,25} The sulfur of one of the bridging cysteines (Cys549) is hydrogen-bonded to the N_ϵ of a histidine (His88). (b) Overview of the SOMO from the DFT calculation of a truncated model for the active site in the oxidized state (model 2 in the Materials and Methods section). The contour of the nickel $3d_{z^2}$ orbital is visible; additional spin density is found in the $3p_z$ orbital of S_γ (Cys549) (bridging cysteine).

* Author to whom correspondence should be addressed. Phone: ++49-208-306-3614. Fax: ++49-208-306-3955. E-mail: lubitz@mpi-muelheim.mpg.de.

is proposed to occur, leading to another EPR-silent “active” state, called Ni-SIa.^{9,12,13} After another one-electron reduction,

the site is EPR-active again, and its EPR signal, called Ni-C, is characterized by g tensor components of 2.20, 2.14, and 2.01, respectively. Last, another one-electron reduction leads to the fully reduced EPR-silent state, which is called Ni-R.^{9,12,13}

EPR spectroscopy combined with density functional theory (DFT) calculations have been instrumental in determining the identity of the additional (third) bridging ligand between Ni and Fe in the various paramagnetic states of the enzyme. In the oxidized Ni-B state a hydroxo (OH^-) bridge has been identified.¹⁴ In Ni-A a hydroperoxo (OOH^-) ligand has been proposed in recent X-ray crystallographic work,^{15,16} but a corroboration by spectroscopic techniques is still lacking. In the reduced state of the enzyme, EPR, electron nuclear double resonance (ENDOR), and hyperfine sublevel correlation (HYSCORE) experiments showed that the bridging ligand is a hydride (H^-).^{17,18} The g values determined from EPR studies^{19–26} and theoretical descriptions based on DFT calculations^{27–33} are all compatible with an electronic structure in which the unpaired electron mainly resides in a $3d_z^2$ orbital on nickel in the paramagnetic Ni-A, Ni-B, and Ni-C states. In the calculations, the $3p_z$ orbital of the cysteine opposite to the free coordination position of Ni (Cys549 in *D. vulgaris* Miyazaki F hydrogenase) also carries significant spin density. This cysteine occupies the axial position of the square pyramidal ligand field environment of the Ni. A small amount of spin density is also present on the sulfur of Cys546. A picture of the orbital of the unpaired electron (SOMO) for the Ni-B redox state is given in Figure 1b.

From the observation that the wave function of the unpaired electron is delocalized over nickel and $\text{S}_\gamma(\text{Cys549})$, it is clear from ligand field theory that the energies of the $\text{Ni}(3d)$ and $\text{S}_\gamma(3p)$ orbitals are similar. It is therefore likely that even small effects of the environment can have a significant impact on the delocalization of the spin density, which might affect the spectroscopic and functional properties of the active site. Inspection of the X-ray crystallographic structure of the oxidized and reduced forms^{2,3} shows that a possible effect might come from the presence of a hydrogen bond between $\text{S}_\gamma(\text{Cys549})$ and $\text{N}_\epsilon(\text{His88})$. This histidine is conserved in all known catalytic [NiFe] hydrogenases.^{1,34} The hydrogen bond places a positive partial charge of the proton near the sulfur atom, which stabilizes the sulfur $3p$ orbitals with respect to the $\text{Ni}(3d)$ orbitals. The existence of this hydrogen bond has already been proposed based on the X-ray structural data³⁵ and electron spin-echo envelope modulation (ESEEM) studies³⁶ of the enzyme from *D. gigas*, but its effect on the electronic structure of the active site has not been investigated. In another publication, the regulatory hydrogenase (RH) of *Ralstonia eutropha* was studied, which has a glutamate instead of a histidine in this position. A mutation from Glu to His in this species leads to the formation of a hydrogen bond that has been detected and studied by pulse EPR spectroscopy.³⁷

The formation of the hydrogen bond affects the electronic structure of the paramagnetic [NiFe] site and is reflected in a coupling of the hydrogen of the hydrogen-bond donor, i.e., the $\text{N}_\epsilon\text{—H}$ group of His88. In addition to the hydrogen the respective nitrogen nuclear spin can be used as a natural spin probe to detect the coupling with the histidine. It is known from ESEEM³⁸ and nuclear quadrupole resonance (NQR)^{39–42} experiments that the quadrupole interaction of ^{14}N in imidazoles is largely determined by the strength of the hydrogen bond formed by the imidazole N—H to a hydrogen-bond acceptor. Thus, the measurement of this interaction yields information on the hydrogen-bond strength. Moreover, the determination of the hyperfine interaction of the unpaired electron and the nitrogen

nuclear spin gives direct information about the amount of delocalization of the wave function over Ni, $\text{S}_\gamma(\text{Cys549})$, and His88.

In this work we aim to determine the strength of the hydrogen bond between His88 and Cys549 in the Ni-B redox state by ESEEM and HYSCORE spectroscopy in combination with DFT calculations. To assign the resonances to histidine and to obtain accurate values for the nuclear hyperfine and quadrupole parameters, measurements have been performed both on the native ^{14}N histidine ($I^{14}\text{N} = 1$) and on ^{15}N -histidine-enriched samples. The ^{15}N isotope has a nuclear spin $I = 1/2$ and lacks the quadrupole interaction. From simulations of the spectra of the enriched sample, hyperfine parameters have been extracted with high accuracy (± 0.1 MHz). These parameters have been kept fixed in the simulation of the spectra recorded on samples with the native ^{14}N isotope, which facilitates the exact determination of the quadrupole parameters. From the DFT calculations, estimates can be obtained for the effect of the hydrogen bond strength between the histidine and the bridging cysteine sulfur of the active site. In turn, this is expected to give information on the impact of the hydrogen bond on the electronic properties of the [NiFe] center.

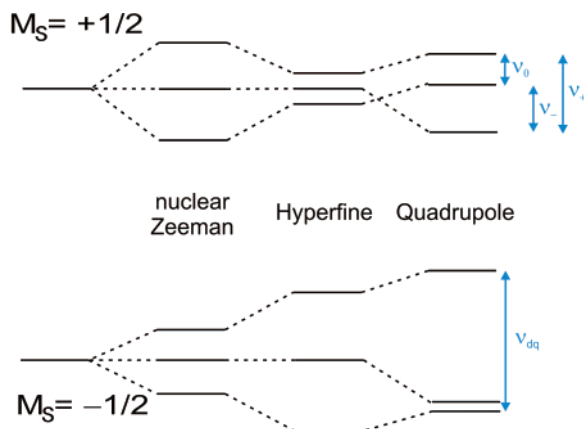
Materials and Methods

Sample Preparation. Cell cultures were grown on a minimal medium with a composition of 0.5 g/L KH_2PO_4 , 4.5 g/L Na_2SO_4 , 0.04 g/L $\text{CaCl}_2 \cdot 2\text{H}_2\text{O}$, 0.06 g/L $\text{MgSO}_4 \cdot 7\text{H}_2\text{O}$, 0.3 g/L sodium citrate and 20 mL of sodium lactate (25% v/v). After the medium was autoclaved, 0.01 g/L FeSO_4 (1 mL of the stock solution), 5 mL of each amino acid stock, 1 mL of trace element stock, 1.3 mg/L NiCl_2 , and 5 mL of 10% antifoam were added to 8 L of media. The amino acid stock solution I (soluble at neutral pH) contained 10 g/L Ala, 4 g/L Arg, 2 g/L Cys, 4 g/L Gly, 1 g/L Lys, 4 g/L Met, 6 g/L Pro, 6 g/L Ser, 8 g/L Thr, and 2 g/L Trp. Amino acid stock solution II (soluble at alkaline pH) contained 8 g/L Asp, 16 g/L Glu, 2 g/L His, 8 g/L Leu, 6 g/L Phe, 8 g/L Tyr, and 8 g/L Val. The trace element stock solution contained 1.5 g/L $\text{FeCl}_2 \cdot 4\text{H}_2\text{O}$, 60 mg/L H_3BO_3 , 120 mg/L $\text{CoCl}_2 \cdot 6\text{H}_2\text{O}$, 70 mg/L ZnCl_2 , 15 mg/L $\text{CuCl}_2 \cdot 2\text{H}_2\text{O}$, and 25 mg/L $\text{NaMoO}_4 \cdot 2\text{H}_2\text{O}$. For ^{15}N His labeling, normal His in amino acid stock solution II was replaced by ^{15}N His (98%, labeled at all three positions) purchased from Cambridge Isotope Laboratories, Inc.

A homemade, 10 L glass fermentor was used for scaling up the cultures. The cell growth and protein purification procedures used were the same as those described in ref 43. The concentration of the protein was determined by a Bradford assay.⁴⁴ A protein concentration of 700 μM was used for all experiments. The as-isolated protein is a mixture of Ni-A and Ni-B. To prepare pure Ni-B for EPR measurements, a 100 μL aliquot of the oxidized (as-isolated) protein was first reduced by bubbling with H_2 for 2 h in an X-band EPR tube with constant stirring in a 37 $^\circ\text{C}$ water bath. Subsequently the samples were oxidized for 2 min by letting air into the sample tube at room temperature. This resulted routinely in an enrichment of the Ni-B state of about 85%.

Instrumentation. Continuous wave (cw) EPR spectra were recorded at $T = 120$ K on a Bruker E500 ELEXSYS EPR spectrometer equipped with an Oxford flow-cryostat CF 935. The microwave frequency was 9.70 GHz, and the modulation amplitude and frequency were 0.5 mT and 100 kHz, respectively. The three-pulse ESEEM ($\pi/2\text{—}\tau\text{—}\pi/2\text{—}t\text{—}\pi/2\text{—}\tau\text{—}\text{echo}$) and HYSCORE ($\pi/2\text{—}\tau\text{—}\pi/2\text{—}t_1\text{—}\pi\text{—}t_2\text{—}\pi/2\text{—}\tau\text{—}\text{echo}$) experiments were recorded at $T = 5$ K on a Bruker ESP 380 E FT-

SCHEME 1: Energy Level Diagram for a ^{14}N Nuclear Spin ($I = 1$) in an External Magnetic Field Interacting with an Unpaired Electron Spin ($S = 1/2$) for the Case $|A| \approx 2\nu_n$.



EPR spectrometer equipped with a dielectric ring resonator (ESP 380-1052 DL Q-H). The separation of the first and second microwave pulses was 144 ns. The length of the 90° pulses was 16 ns, and for HYSCORE, that of the 180° pulse was 24 ns. In total, 512 and 256×256 data points were recorded in the ESEEM and HYSCORE experiments. The microwave frequency was 9.70 GHz, the time increments of the t (ESEEM) or t_1 and t_2 (HYSCORE) times were 16 ns, and the shot repetition time was 10.24 ms. The resulting modulation pattern was baseline-corrected, a Hamming window function was used for apodization, and the array was increased to 4096 (ESEEM) or 1024×1024 (HYSCORE) points by zero-filling. Then the array was Fourier-transformed into the frequency domain. All spectra shown here are magnitude spectra. No dead time reconstruction procedures were used.

Evaluation of Spectra. Simulations of the ESEEM and HYSCORE spectra have been performed with software of which a description is given in refs 45 and 17. For ^{14}N , the nuclear transition frequencies of nitrogen are given by the energy level diagram in Scheme 1.

When the nuclear Zeeman frequency ν_n is about equal to half of the effective hyperfine coupling constant A , these interactions cancel each other in one M_S manifold,⁴⁶ and three sharp nuclear transition frequencies ν_0 , ν_- , and ν_+ are obtained representing the zero-field quadrupole transitions.⁴⁷ From these frequencies, $\nu_{\pm} = K(3 \pm \eta)$ and $\nu_0 = 2K\eta$, the principal values of the quadrupole tensor $[K(\eta - 1), -K(\eta + 1), 2K]$ ⁴⁸ are obtained, where K is the quadrupole coupling parameter, $K = e^2qQ/4h$. From the other M_S manifold only the largest, double-quantum frequency is usually observed. This frequency can be written as⁴⁹

$$\nu_{dq} = 2 \left[\left(\frac{|A|}{2} + \nu_n \right)^2 + K^2(3 + \eta^2) \right]^{1/2}$$

In these equations the parameters $e^2qQ/h = 4K$ and η indicate the size and the symmetry of the quadrupole interaction. They are related to the electric quadrupole coupling tensor P of the respective nucleus (with components P_i , $2P_z = e^2qQ/h$, $\eta = (P_y - P_x)/P_z$ with $|P_z| > |P_y| \geq |P_x|$). In three-pulse ESEEM spectra, the four frequencies ν_0 , ν_- , ν_+ , and ν_{dq} are usually observed for the ^{14}N nucleus. In the ^{14}N HYSCORE spectra, correlations are expected between ν_{dq} and ν_0 , ν_- , or ν_+ . For the ^{15}N isotope ($I = 1/2$) the energy level diagram in Scheme 1

simplifies to a four-level diagram, and only one nuclear frequency per M_S manifold is present. Out of the two nuclear transition frequencies, in ESEEM, only the small frequency (usually lying below 1 MHz) has a nonnegligible intensity.⁴⁵ In the HYSCORE spectrum, a correlation peak is observed between the two ^{15}N transition frequencies of the $M_S = +1/2$ and $M_S = -1/2$ states. Whereas ESEEM spectra are sometimes difficult to interpret because they are one-dimensional spectra, a combined simulation of HYSCORE and ESEEM spectra of the labeled and unlabeled hydrogenase allows for accurate assignment of the nuclear frequencies and subsequently elucidation of the nuclear hyperfine and quadrupole coupling constants.

DFT Calculations. All DFT calculations were performed with the ORCA programming package.⁵⁰ The B3LYP functional was used within a spin-unrestricted formalism. Two model systems were considered. The model system 1 of the active site consists of Ni, Fe, four $\text{CH}_3\text{CH}_2\text{S}^-$ groups to model the cysteines, the diatomic ligands of iron (two CN^- and one CO), and the bridging OH^- ligand. Model 2 additionally includes a methylimidazole group to model His88 (Figure 1).¹⁴ Model 2 was optimized using constrained geometry optimizations in which the α carbons of the four cysteines and the C_γ and N_δ of His88 were kept fixed as in the X-ray structure. After geometry optimization, the Ni–S distances were manually adjusted to 2.22 Å, based on data from extended X-ray absorption fine structure measurements,⁵¹ as DFT geometry optimization is known to be less accurate in optimizing metal–sulfur distances.⁵² Further details concerning basis set and convergence criteria are identical to those described in ref 14. The error margin of the DFT method with respect to calculating g values is about 30% in the g shift ($\Delta g_i = g_i - g_e$)^{28,53} and about 20% for the ligand hyperfine interactions.⁵⁴ For the largest g value, g_x , the DFT calculations are known to systematically underestimate the experimental g value.⁵³ For the central metal, especially the isotropic hyperfine interaction is difficult to calculate.⁵⁴ Spin contamination was found to be minor, and $\langle S^2 \rangle$ values around 0.77 were found, which deviates only slightly from the ideal values of $\langle S^2 \rangle = S(S + 1) = 0.75$ for an $S = 1/2$ system.

Results and Discussion

EPR. The continuous wave (cw) EPR powder spectrum of a frozen solution of ^{15}N -histidine-enriched [NiFe] hydrogenase of *D. vulgaris* Miyazaki F is shown in Figure 2. The sample has been prepared in such a way as to maximize the amount of the Ni-B redox state. The g tensor components of the Ni-B state read from the spectrum are $g_x = 2.33$, $g_y = 2.16$, and $g_z = 2.01$, in agreement with those measured earlier by EPR spectroscopy on this hydrogenase in single crystals^{26,55} and also on other [NiFe] hydrogenases.^{56,57} In the sample a small amount of the Ni-A state is still present. From a simulation of the spectrum, included in Figure 2, a ratio of Ni-B/Ni-A of about 85:15 is determined. This is sufficient for the accurate elucidation of hyperfine and quadrupole parameters of Ni-B from EPR related techniques such as ESEEM and HYSCORE spectroscopy.

ESEEM and HYSCORE. The three-pulse ESEEM spectra for *D. vulgaris* Miyazaki F hydrogenase in the Ni-B state with ^{14}N histidine and with ^{15}N labeled histidine recorded at three different magnetic field settings are shown in Figure 3. The magnetic field settings at which the spectra were obtained correspond to the g_x and g_y canonical orientations and $g = 2.05$. The latter magnetic field setting was chosen as close as possible to the g_z canonical orientation without interference with the signal from the [3Fe4S] cluster. The spectra with unlabeled (^{14}N) histidine display three bands, denoted ν_0 , ν_- , and ν_+ , with

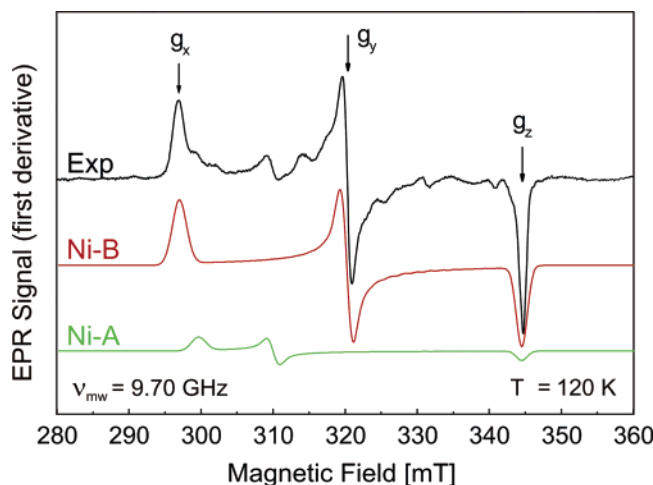


Figure 2. Continuous wave EPR powder spectrum of ^{15}N -histidine-enriched *D. vulgaris* Miyazaki F hydrogenase, which contains predominantly the Ni-B redox state. The respective Ni-B spectrum with ^{14}N histidine was virtually identical to this trace; i.e., no distinction can be made based on the EPR spectra alone. Experimental conditions: $T = 120\text{ K}$, $\nu_{\text{mw}} = 9.70\text{ GHz}$, modulation amplitude = 0.5 mT , microwave power $P_{\text{mw}} = 1.54\text{ mW}$. The middle and lower traces are simulations for the Ni-B (85%) and Ni-A (15%) redox states. For g tensor values, see text.

frequencies of about 0.4, 1.2, and 1.6/1.7 MHz, which are characteristic of nuclear quadrupole single quantum frequencies of ^{14}N (Materials and Methods).⁴⁷ The frequencies of these bands remain constant to within 0.1 MHz when the magnetic field setting is changed, but their relative intensities change. At around 4 MHz, a broad and weak signal with a poorly resolved structure is visible, which corresponds to the double-quantum transition (ν_{dq}) of the noncanceled manifold. The structure of this transition is caused mainly by the anisotropy of the hyperfine tensor (vide infra). In the ESEEM spectra of the ^{15}N -histidine-enriched sample, the intensity of the bands in the spectrum is reduced dramatically. For ^{15}N ($I = 1/2$), no quadrupole interaction is present, and only two transitions, one per M_S manifold, are expected. The amplitudes of the bands that belong to these transitions are very small in the ESEEM spectra, but they can be observed more easily by HYSCORE spectroscopy (see below). The changes in the ESEEM spectra upon ^{15}N histidine labeling show that the observed signals in the native sample indeed result from a histidine nitrogen.

HYSCORE spectra recorded under the same experimental conditions as the ESEEM spectra are presented in Figure 4. The spectra in the left column were obtained for the natural abundance ^{14}N histidine sample, whereas the spectra in the right column stem from the ^{15}N -enriched histidine sample. Comparison of the experimental spectra in the two columns reveals significant differences. The spectrum with ^{15}N -enriched histidine shows two strong cross-peaks at (0.5, 2.5) MHz and (2.5, 0.5) MHz. The transitions at 0.5 and 2.5 MHz are the ^{15}N nuclear transitions of the $M_S = +1/2$ and $-1/2$ manifolds. The spectrum with natural abundance ^{14}N histidine displays a richer structure with cross-peaks at (1.2, 4.1), (1.7, 4.1), (0.4, 4.1), (4.1, 1.2), (4.1, 1.7), and (4.1, 0.4) MHz. Each cross-peak relates one of the single quantum spin transitions (ν_0 , ν_- , or ν_+) to the double-quantum transition (ν_{dq}) of the noncanceled manifold. Similar to the case of the ESEEM spectra, the positions of the cross-peaks do not change much with magnetic field, but their relative intensities vary when going from g_x to $g = 2.05$. A small amount of the ^{14}N signal can still be observed in the ^{15}N -enriched spectra. The signals on the diagonal stem from the three-pulse

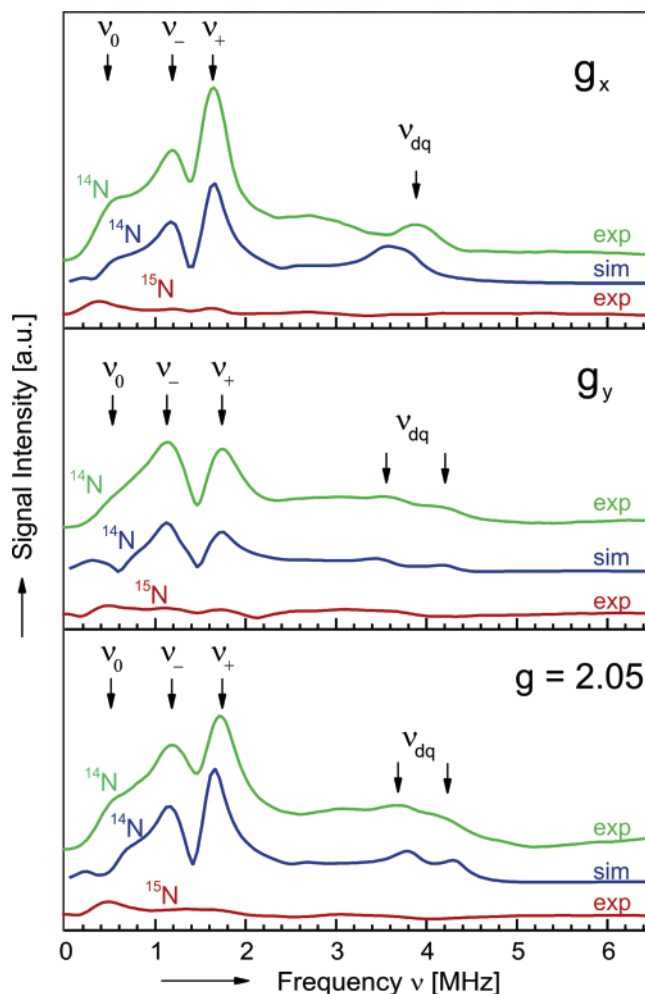


Figure 3. Three-pulse ESEEM spectra and simulations for *D. vulgaris* Miyazaki F hydrogenase in the Ni-B redox state recorded at the g_x and g_y canonical orientations and $g = 2.05$, close to g_z : green traces, spectra of the nonenriched (^{14}N histidine) sample; blue traces, simulation of the spectra of the nonenriched sample; red traces, spectra of the ^{15}N -histidine-enriched sample. For experimental details, see the Materials and Methods section; for simulation parameters, see Table 1.

stimulated echo due to incomplete population inversion of the 180° microwave pulse.

The changes in the HYSCORE spectra upon labeling of the protein with ^{15}N histidine also confirm that the signals in the $^{14}\text{N}/^{15}\text{N}$ region indeed stem from a histidine nitrogen. From the cross-peaks in the ^{14}N spectra, the three quadrupole frequencies already observed in the ESEEM spectra are again found to be 0.4, 1.2, and 1.6/1.7 MHz. The values are in agreement with the assignment of this nitrogen as an imidazole N_ϵ nitrogen.^{37,38} A similar pattern has also been observed for *D. gigas* hydrogenase,³⁶ for which it was already suggested that the nitrogen signals are possibly from a histidine coupled to the nickel center. The line widths of the signals in ref 36 are narrower than that observed here, since the lower microwave frequency used in this work brings the nitrogen closer to fulfilling the exact cancellation condition.⁴⁷ Further evidence for the assignment to His88 comes from mutagenesis studies on the regulatory hydrogenase of *R. eutropha*,³⁷ which has a glutamate at the respective position in the sequence and does not exhibit nitrogen modulations. When the glutamate was changed to histidine, an ESEEM spectrum similar to that reported here was observed.³⁷

To extract more accurate hyperfine and quadrupole parameters for the nitrogen, the spectra in the $^{14}\text{N}/^{15}\text{N}$ region have been simulated. First, the hyperfine coupling constants were eluci-

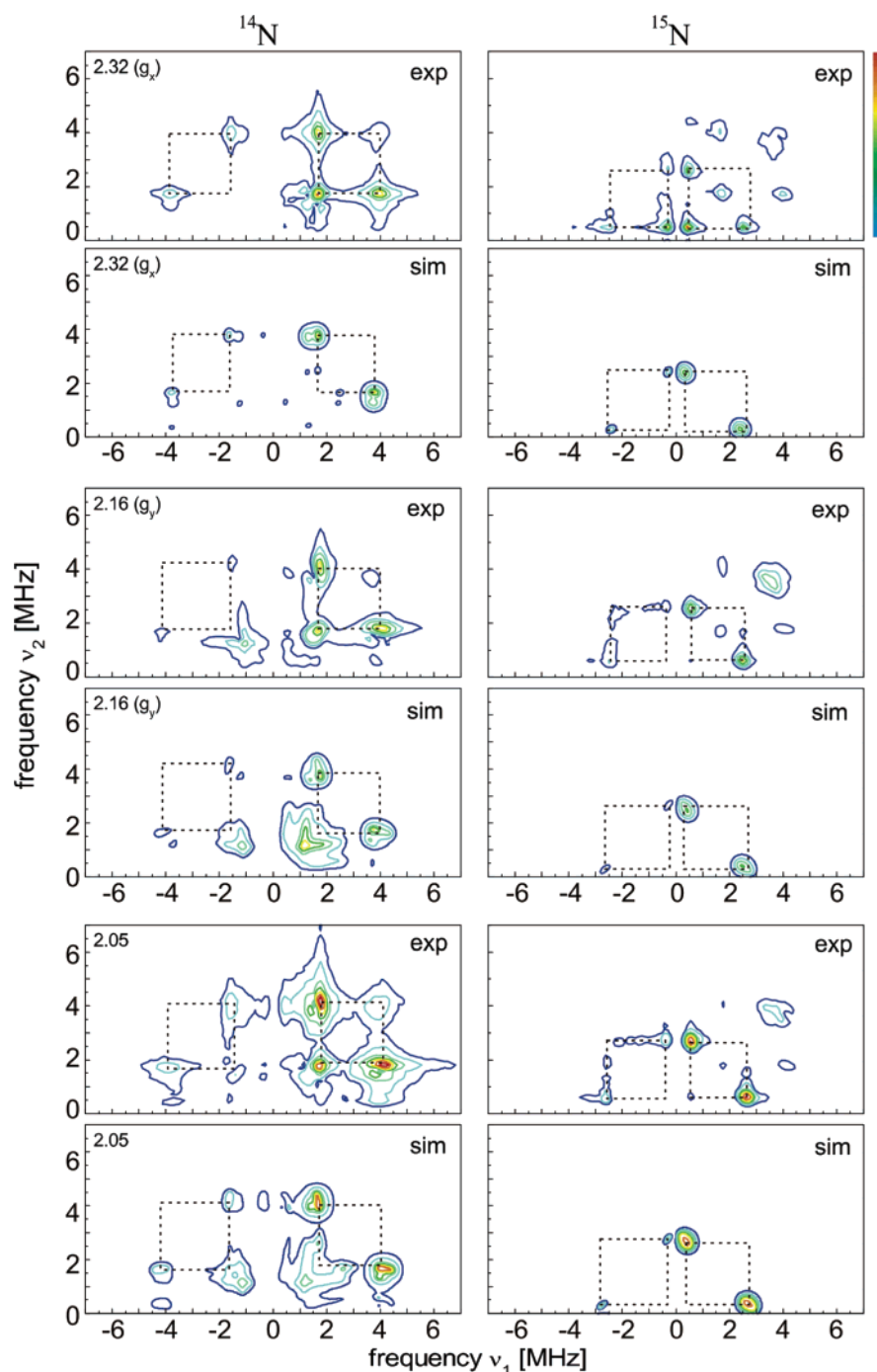


Figure 4. HYSCORE spectra (—+ and ++ quadrants) of *D. vulgaris* Miyazaki F hydrogenase in the Ni-B redox state recorded at the g_x and g_y canonical orientations and at $g = 2.05$. The respective simulations are also shown: left column, natural abundance (^{14}N) histidine sample; right column, ^{15}N -histidine-enriched sample. The g values at which the spectra were recorded are indicated in the left diagrams. For experimental details, see the Materials and Methods section; for simulation parameters, see Table 1. In the ^{15}N histidine sample, bands are visible from a small amount of ^{14}N left in the sample. ^{14}N has a much larger modulation depth than the ^{15}N isotope (Figure 3). Cross-peaks of fundamental frequencies are indicated by dotted lines.

dated by simulation of the ^{15}N HYSCORE spectra ($I = 1/2$), since the ^{15}N nucleus lacks the quadrupole interaction. The simulations are included in Figure 4. Since little intensity is present in the corresponding ESEEM spectra (Figure 3), the ESEEM simulations for the ^{15}N -histidine-enriched sample are not shown. From both the positions and the line shapes of the cross-peaks, accurate principal values (± 0.1 MHz) could be determined. The ^{14}N hyperfine tensor was found to have an isotropic hyperfine coupling constant of 1.57 MHz (converted from the ^{15}N hyperfine couplings using the gyromagnetic ratios of ^{14}N and ^{15}N $\gamma^{15\text{N}}/\gamma^{14\text{N}} = 1.403$). The anisotropic part of the

tensor was found to be axial, with the largest component being $A_z' = 0.50$ MHz. The parameters, valid for the ^{14}N isotope, are summarized in Table 1. The direction of the dipolar axis was determined relative to the principal axes of the g tensor⁵⁵ with an accuracy of approximately $\pm 15^\circ$. The A_z -axis makes an angle of 12° with the $\text{N}_\epsilon\text{--S}_\gamma$ direction in the X-ray structure.²

Subsequently, nuclear quadrupole coupling constants were extracted from the HYSCORE spectrum of the ^{14}N sample. In this simulation the hyperfine tensor was kept fixed, and the quadrupole tensor was optimized. Starting parameters for the principal axes of the quadrupole tensor were chosen such that

TABLE 1: ^{14}N Hyperfine and Quadrupole Coupling Constants for the N_ϵ of His88 in *D. vulgaris* Miyazaki F [NiFe] Hydrogenase in the Ni-B State^a

	^{14}N hyperfine coupling constants				^{14}N quadrupole coupling constants					
	A	I_{ai}	I_{bi}	I_{ci}	P_i	I_{ai}	I_{bi}	I_{ci}		
a_{iso}	+1.57				e^2qQ/h	−1.90				
A'_x	−0.25				η	0.37	P_x	+0.30	−0.008	−0.999
A'_y	−0.25						P_y	+0.65	+0.325	−0.044
A'_z	+0.50	+0.470	+0.881	−0.100			P_z	−0.95	−0.946	−0.013
										+0.327

^a The principal values and principal axes of the hyperfine tensor have been obtained by simulation of the ^{15}N HYSCORE spectra. ($\gamma^{15}\text{N}/\gamma^{14}\text{N} = 1.403$). The hyperfine parameters were kept fixed in the subsequent optimization of the simulation of the ^{14}N HYSCORE spectra, from which the quadrupole coupling constants were obtained. The directions of the principal axes I_{ji} ($i = x, y, z$) are given in the crystallographic axes system ($j = a, b, c$). Note that the negative sign of e^2qQ/h is inferred from calculations of the electric field gradient⁴⁰ ($e^2qQ/h = 2P_z$, $\eta = |(P_x - P_y)/P_z|$).

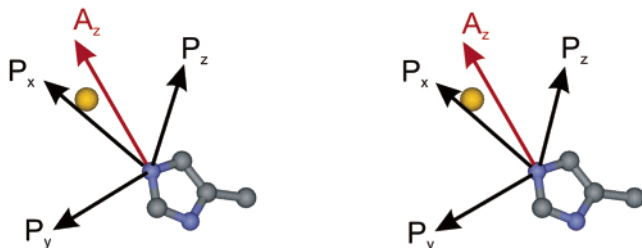


Figure 5. Stereoview of the directions of the principal axes of the quadrupole tensor and the dipolar axis of the hyperfine tensor (A_z), as elucidated from the ESEEM and HYSCORE spectra for ^{14}N - and ^{15}N -histidine-enriched samples. The sulfur atom of Cys549 is indicated in yellow. The A_x and A_y directions are not given, because the hyperfine tensor is axially symmetric. The coordinates of the atoms are taken from the X-ray structure.²

the principal P_x -axis (corresponding to the smallest absolute principal value) is parallel to the histidine $\text{N}_\epsilon\text{—H}$ direction and the principal P_z -axis (corresponding to the largest absolute principal value) is perpendicular to the imidazole plane. This choice of tensor axes is based on the extensive work in refs 39 and 58. Only minor adjustments were necessary. The optimized parameters are included in Table 1, and the simulations are shown in Figures 3 (center traces) and 4. The magnitude of the quadrupole coupling e^2qQ/h (-1.90 ± 0.05 MHz) is equal to that estimated from the ESEEM spectra for *D. gigas* hydrogenase.³⁶ The directions of the principal axes are shown schematically in Figure 5. After optimization, the angle between the P_x principal axis and the $\text{N}_\epsilon\text{—S}$ direction as given in the X-ray structure is 26° . The angle between the P_z -axis and the normal to the imidazole plane is also close to 26° . It is known that the P_x - and P_z -axes for the imidazole nitrogen are oriented approximately parallel to the $\text{N}_\epsilon\text{—H}$ direction and perpendicular to the imidazole plane, respectively.⁵⁸ In our DFT calculations (vide infra) an angle of 17° is found between the P_x -axis and the $\text{N}_\epsilon\text{—S}$ bond direction, and 11° between the P_z -axis and the normal to the imidazole plane. Considering the accuracy with which the quadrupole axes are determined from the ESEEM and HYSCORE spectra ($\pm 15^\circ$) and the resolution of the crystallographic structures,^{2,59} the experimental and calculated orientations of the quadrupole axes are in satisfying agreement.

No attempts were made to simulate the ESEEM signals on the diagonal in the HYSCORE spectra. For both ^{14}N and ^{15}N the simulations satisfactorily reproduce both the position and the line shape of the bands in the ESEEM spectra and the cross-peaks in the HYSCORE spectra. The largest mismatch between simulation and experiment occurs at the single-crystal-like g_x canonical orientation. At this orientation the simulated double-quantum transition is about 0.2 MHz too low as compared to the experiment. Most probably, the reason for the mismatch is that the simulations at single-crystal-like positions are more

TABLE 2: Overview of g Values and Mulliken Spin Densities (in %) from DFT Calculations of the Model Systems 1 and 2 of the Active Site of *D. vulgaris* Miyazaki F Hydrogenase in the Ni-B State^a

	1	2
g_x	2.21	2.23
g_y	2.15	2.18
g_z	2.03	2.03
$\rho(\text{Ni})$	75.2%	82.3%
$\rho(\text{S}_\gamma(\text{Cys549}))$	28.4%	21.5%
$\rho(\text{S}_\gamma(\text{Cys81}))$	−3.7%	−4.4%
$\rho(\text{N}_\epsilon(\text{His88}))$		0.14%
$\rho(\text{N}_\delta(\text{His88}))$		0.01%

^a The spin densities are total spin densities (sum of all s, p, and d orbitals). Note that the s spin density at the nitrogen atoms, responsible for the isotropic hyperfine coupling constants, is 0.68% and -0.002% for the N_ϵ and N_δ , respectively.

sensitive to how the excitation bandwidth of the microwave pulses, or g strain effects, are modeled.⁴⁵ (Likewise, the experimental spectra also change the most at single-crystal orientations when a different excitation bandwidth is chosen.)

DFT Calculations. To complement the experimental data, DFT calculations have been performed on a truncated model system of the [NiFe] site (for details, see Materials and Methods). Two calculations have been performed, one without and one with a methylimidazole, which models the His88 residue of the large subunit. For the larger model (2), a distance $d(\text{N}_\epsilon(\text{His88})\text{—S}_\gamma(\text{Cys549}))$ of 3.38 Å is found in the constrained geometry optimization. A full geometry optimization resulted in a distance of 3.40 Å. These values are more or less the average of those found for *D. vulgaris* Miyazaki F² (3.27 Å) and *D. gigas*⁶⁰ (3.48 Å). On the basis of the similarity of the quadrupole parameters obtained here and for *D. gigas* hydrogenase (in the oxidized Ni-A state),² we believe that the difference of the two X-ray distances reflects the accuracy of the Cartesian coordinates of the atoms in the respective X-ray structures, which is about ± 0.1 Å. The constraints in the geometry optimization were necessary to keep the outer atoms of the model from rotating too far away from their initial X-ray positions, which is a crude way of taking the geometry constraints imposed by the protein into account. Another observation when examining the X-ray structure is that the $\text{N}_\epsilon\text{—H}\cdots\text{S}$ bond is not completely linear. This is unexpected and might indicate a certain degree of flexibility of the His88 in forming the hydrogen bond. This may lead to a distribution of hydrogen-bond conformations and strengths.

The calculated g values and spin densities are given in Table 2, and a selection of hyperfine coupling constants in Table 3. As is obvious from the tables, the calculations show that the only nitrogen that is close enough to the active site to be compatible with the ^{14}N hyperfine coupling constants is the ϵ

TABLE 3: Overview of the Hyperfine Coupling Constants (MHz) from DFT Calculations of the Model Systems 1 and 2 of the Active Site of *D. vulgaris* Miyazaki F Hydrogenase in the Ni-B State

	⁶¹ Ni ^a		³³ S _γ (Cys549)		¹⁷ O(OH [−] bridge) ^a		¹ H(OH [−] bridge)		¹ H _ε (His88)		¹⁴ N _ε (His88) ^b		¹⁴ N _δ (His88) ^c	
	1	2	1	2	1	2	1	2	1	2	1	2	1	2
<i>a</i> _{iso}	−58.4	−80.0	+39.2	+48.2	−8.16	−8.29	−1.44	−1.21	−0.94		+2.20		−0.01	
<i>A</i> ' _x	+44.2	+41.5	−28.3	−20.7	+4.74	+4.41	−4.86	−4.95	−3.09		−0.24		−0.04	
<i>A</i> ' _y	+16.1	+18.0	−27.1	−22.3	+3.19	+2.69	−3.35	−3.59	−2.32		−0.22		−0.02	
<i>A</i> ' _z	−60.3	−59.5	+55.3	+43.0	−7.92	−7.10	+8.21	+8.54	+5.41		+0.46		+0.06	

^a Note that ⁶¹Ni and ¹⁷O have negative nuclear *g* values. ^b The calculated nuclear quadrupole parameters for ¹⁴N_ε(His88) are $e^2qQ/h = -2.18$, $\eta = 0.43$. ^c The calculated nuclear quadrupole parameters for ¹⁴N_δ(His88) are $e^2qQ/h = -3.80$, $\eta = 0.12$.

nitrogen of His88. The hyperfine coupling constants for the δ nitrogen are much smaller than those for N_ε. The CN[−] nitrogens also have hyperfine coupling constants of less than ~ 0.1 MHz.

When focusing on the impact of the histidine and the hydrogen bond to the sulfur (Cys549) on the electronic structure of the active site, a striking difference is observed when comparing the spin density distribution of the models without and with the inclusion of histidine. The spin densities at nickel and S_γ(Cys549) are 75.2% and 28.4% without the histidine and 82.3% and 21.5%, respectively, with the histidine. Obviously, the presence of the hydrogen-bond-forming histidine residue in the calculation shifts a significant fraction of spin density from sulfur to nickel, i.e., 6–7%. This can be understood on the basis of ligand field theory. The nickel orbitals are slightly higher in energy than the sulfur orbitals. With the histidine, a partial positive charge (δ^+) of the hydrogen-bonded proton at N_ε is present near S_γ(Cys549). This stabilizes the sulfur 3p orbitals such that the energy gap between the sulfur and the nickel orbitals increases. The sulfur orbitals will mix less into the wave function of the unpaired electron, and the spin density shifts to the nickel side. For an accurate theoretical description of the electronic structure of the [NiFe] site, it is therefore important to include the hydrogen bond to S_γ(Cys549), which fine-tunes the relative energies of the Ni and S orbitals.

The effect of other nearby amino acids was investigated as well. Calculations have been performed on the model with His88 including the nearby Glu34, Arg479 (modeled as a cation), or Ser502 amino acids; see Figure 1a. Since these amino acids are further away from both Ni and S(Cys549) they are expected to have a smaller effect on the delocalization of spin density over Ni and S(Cys549). This was indeed found to be the case. In a calculation in which His88 and the other three amino acids were included, the shift in spin density caused by the inclusion of His88 was compensated for by the presence of the other amino acids to about 50%. The reason for this is that the other amino acids are closer to Ni, i.e., in positions that stabilize the Ni(3d) orbitals instead of the sulfur 3p orbitals.

When examining the calculated ¹H hyperfine coupling constants in the large model (2), the proton with the largest anisotropic coupling is that of the OH[−] ligand that forms the bridge between Ni and Fe, for which *a*_{iso} = −1.21 MHz and *A*'_z = +8.54 MHz were found.¹⁴ The ϵ proton of His88, which forms the hydrogen bond, has a smaller isotropic hyperfine coupling constant (−0.94 MHz), and the largest component of the anisotropic hyperfine interaction is *A*'_z = +5.41 MHz. This proton shows the second largest calculated anisotropic ¹H hyperfine interaction. It is, however, very difficult to directly detect this proton with ESEEM or ENDOR spectroscopy and extract accurate hyperfine coupling constants, as the signal falls in a region where it overlaps with that of the six β protons of the equatorial cysteines.¹⁴

The isotropic hyperfine coupling constant of ¹⁴N_ε(His88) is calculated to be somewhat larger (*a*_{iso} = +2.20 MHz) than that

elucidated from experiment (*a*_{iso} = +1.57 MHz). The calculated dipolar part of the hyperfine interaction (*A*'_i = −0.24, −0.22, +0.46 MHz) and the experimental dipolar hyperfine coupling constants (*A*'_i = −0.25, −0.25, +0.50 MHz) are, however, in very good agreement. This is indeed very satisfying, taking into account that the nitrogen is located close to the large spin density at S_γ(Cys549). The DFT data strongly support the assignment of the observed nitrogen signals to the N_ε of His88 made in the present work.

The calculated directions of the quadrupole axes are such that the *P*_x principal axis and the N_ε–H direction make an angle of 15°, and the *P*_z principal axis and the normal to the imidazole plane 11°. As was already shown in ref 37, the nuclear quadrupole parameters, especially the asymmetry parameter η , critically depend on the strength of the hydrogen bond. This can be understood since the hydrogen bond affects mainly the *P*_x component and thereby η and to a lesser extent *P*_z = $1/2 e^2 q Q / h$. In ref 37, a model system consisting of an imidazole and an ethanethiol group was used for the DFT calculations. As the nuclear quadrupole interaction is a local property determined by the electronic wave function near the nitrogen, this small model system was expected to sufficiently describe the case of hydrogenase. It was found that the N_δ of His88 is not protonated and the N_ε is.³⁷ In the present work, the ¹⁴N quadrupole tensor of the N_ε of His88 has been calculated in a much larger system that mimics the active site geometry of hydrogenase (Figure 1). For the constrained geometry-optimized structure (*d*(N–S) = 3.38 Å), the following values were obtained $e^2 q Q / h = -2.18$, $\eta = 0.43$. These values, included in Table 3, are in good agreement with experiment (Table 2).

The calculations were performed as a function of the hydrogen-bond distance, by incrementing the distance between Cys549 and His88 and optimizing the position of the proton. A summary of results is shown in Figure 6. The calculated $e^2 q Q / h$ values are smaller than the experimental value. They agree within 0.5 MHz with the experimental value, which is a satisfying agreement for DFT methods. Moreover, since the dielectric constant of a protein at low temperature is not known, it is in general difficult to directly interpret the magnitude (i.e., $e^2 q Q / h$) of the quadrupole interaction. Our calculations are gas-phase calculations ($\epsilon_r = 1$), whereas in another study⁶¹ a value of $\epsilon_r = 2$ was assumed. The asymmetry parameter, which should be independent of the dielectric constant of the medium, can be used for an estimation of the hydrogen-bond length. Agreement between the experimental and the calculated value of η is obtained for an N–S distance of about 3.45 Å. This compares well with the distance found in the X-ray structure of 3.27 Å (ref 2) or 3.48 Å (ref 60) and with the value of 3.38 Å from the constrained geometry optimization. The obtained value agrees with hydrogen bonds to C–S[−] acceptors, which usually lie around 3.3 Å.⁶² Such bonds are formally classified as weak hydrogen bonds.⁶³ This is commonly found for sulfur acceptors.

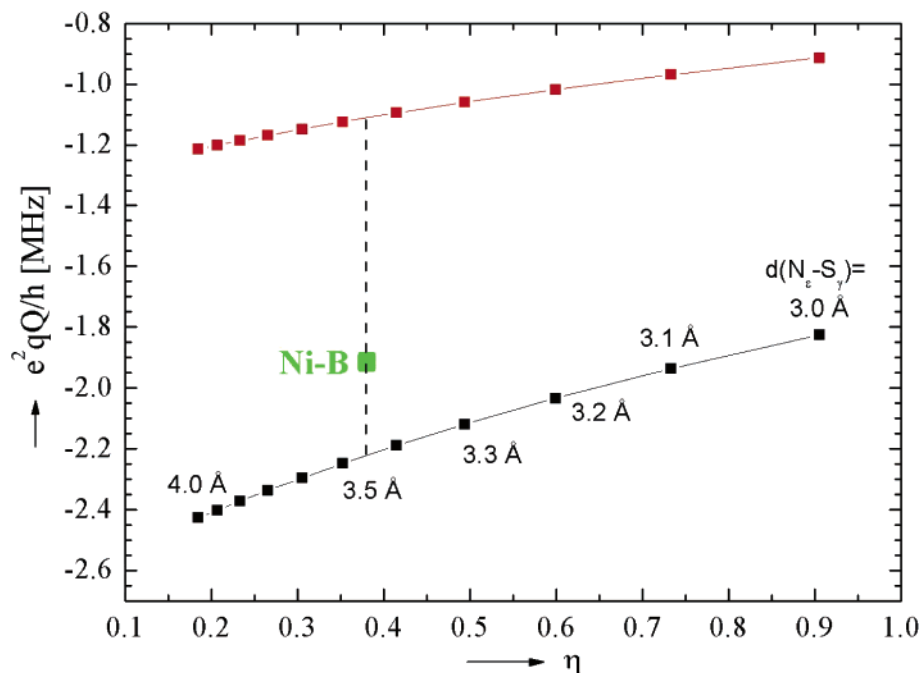


Figure 6. DFT calculated quadrupole parameters for the $^{14}\text{N}_\epsilon$ of His88 as a function of the distance between His88 and Cys549 in the range from 3.0 to 4.0 Å in steps of 0.1 Å. The position of the proton bound to the N_ϵ has been optimized while the $\text{N}_\epsilon\text{--S}_\gamma$ distance was fixed. The calculation is a gas-phase calculation ($\epsilon_r = 1$). In another study, a dielectric constant for proteins⁶¹ was assumed to be 2 (scaled line included in red). Perfect agreement is obtained by choosing $\epsilon_r = 1.2$. The asymmetry parameter η , which is independent of the medium, can be used to estimate the $\text{N}_\epsilon\text{--S}_\gamma$ distance provided an isotropic dielectric constant can be assumed.

A weak hydrogen bond is also found by comparing the experimental values of e^2qQ/h and η with reference data available for imidazole complexes,³⁸ which have been analyzed within a Townes–Daily model. In the Townes–Daily model the p_z orbital and the three sp^2 orbitals at nitrogen are considered as the main source for the electric field gradient at the nucleus. The hydrogen bond is able to polarize the N--H sp^2 orbital to an extent depending on the hydrogen-bond strength. In this comparison it is found that the polarization of the N--H sp^2 orbital is smaller than that in most imidazole compounds. Nevertheless, the hydrogen bond in the [NiFe] hydrogenase is able to fine-tune the spin density distribution of Ni and S.

Summary and Outlook

The hydrogen bond between H_ϵ of His88 and S_γ of Cys549 in the Ni-B state of *D. vulgaris* Miyazaki F hydrogenase has been investigated by ESEEM/HYSCORE spectroscopy and DFT calculations. By experiments on natural abundance samples and ^{15}N -enriched histidine samples, an identification of the nitrogen signals with a histidine imidazole nitrogen (N_ϵ) has been established. From simulations of the spectra, nuclear hyperfine and quadrupole coupling tensors, including tensor orientations, could be elucidated. Comparison with DFT calculations of a truncated model system of the active site shows that the only nitrogen, which is close to the [NiFe] center and has hyperfine coupling constants compatible with those found in the experiment, is the ϵ nitrogen of His88. The quadrupole parameters of this nitrogen allow an estimation of the length of the hydrogen bond between the N_ϵ of His88 and the S_γ of Cys549. Analysis of these parameters leads us to conclude that a hydrogen bond is present at an $\text{N}_\epsilon\text{--S}_\gamma$ distance of about 3.45 Å. This hydrogen bond is able to fine-tune the relative energies of the sulfur orbitals with respect to the nickel orbitals and significantly affects the spin density distribution in the active site. For an accurate description of the [NiFe] center at the electronic level, this hydrogen bond must therefore be included. It can thus be

speculated that the hydrogen bond to the active site is also important for the functional properties of the catalytic enzyme. This can be probed by replacing the His88 in *D. vulgaris* Miyazaki F by other amino acids using site-directed mutagenesis. In this respect it is interesting to notice that the regulatory enzyme, which has a very similar [NiFe] center but does not catalyze hydrogen splitting or production, lacks the histidine and thus this specific hydrogen bond.⁶⁴ The observation that the dynamic movement of His88 modulates the hydrogen-bond interaction and the electronic structure of the active site might be an important aspect for a more detailed understanding of the catalytic cycle.

Acknowledgment. The authors thank Dr. Frank Neese for helpful discussions. Technical assistance by Tanja Berndsen and Gudrun Klihm is gratefully acknowledged. This work was supported financially by the Max Planck Gesellschaft and the EU NEST-STREP RES 516510 (SOLAR-H).

Supporting Information Available: Coordinates of the atoms that comprise the large model (2) used in the DFT calculations. This material is available free of charge via the Internet at <http://pubs.acs.org>.

References and Notes

- (1) Vignais, P. M.; Billoud, B.; Meyer, J. *FEMS Microbiol. Rev.* **2001**, 25, 455–501.
- (2) Higuchi, Y.; Yagi, T.; Yasuoka, N. *Structure* **1997**, 5, 1671–1680.
- (3) Higuchi, Y.; Ogata, H.; Miki, K.; Yasuoka, N.; Yagi, T. *Structure* **1999**, 7, 549–556.
- (4) Fichtner, C. Ph.D. Thesis, Universität Düsseldorf, Germany, 2005.
- (5) Higuchi, Y.; Toujou, F.; Tsukamoto, K.; Yagi, T. *J. Inorg. Biochem.* **2000**, 80, 205–211.
- (6) De Lacey, A. L.; Hatchikian, E. C.; Volbeda, A.; Frey, M.; Fontecilla-Camps, J. C.; Fernandez, V. M. *J. Am. Chem. Soc.* **1997**, 119, 7181–7189.
- (7) George, S. J.; Kurkin, S.; Thorneley, R. N. F.; Albracht, S. P. J. *Biochemistry* **2004**, 43, 6808–6819.

- (8) De Lacey, A. L.; Fernandez, V. M.; Rousset, M.; Cavazza, C.; Hatchikian, E. C. *J. Biol. Inorg. Chem.* **2003**, *8*, 129–134.
- (9) Albracht, S. P. J. *Biochim. Biophys. Acta* **1994**, *1188*, 167–204.
- (10) Fernandez, V. M.; Hatchikian, E. C.; Patil, D. S.; Cammack, R. *Biochim. Biophys. Acta* **1986**, *883*, 145–154.
- (11) Lamle, S. E.; Albracht, S. P. J.; Armstrong, F. A. *J. Am. Chem. Soc.* **2004**, *126*, 14899–14909.
- (12) Bleijlevens, B.; van Broekhuizen, F.; De Lacey, A. L.; Roseboom, W.; Fernandez, V. M.; Albracht, S. P. J. *J. Biol. Inorg. Chem.* **2004**, *9*, 743–752.
- (13) de Lacey, A. L.; Fernandez, V. M.; Rousset, M. *Coord. Chem. Rev.* **2005**, *249*, 1596–1608.
- (14) van Gastel, M.; Stein, M.; Brecht, M.; Schröder, O.; Lendzian, F.; Bittl, R.; Ogata, H.; Higuchi, Y.; Lubitz, W. *J. Biol. Inorg. Chem.* **2006**, *11*, 41–51.
- (15) Volbeda, A.; Martin, L.; Cavazza, C.; Matho, M.; Faber, B. W.; Roseboom, W.; Albracht, S. P. J.; Garcin, E.; Rousset, M.; Fontecilla-Camps, J. C. *J. Biol. Inorg. Chem.* **2005**, *10*, 239–249.
- (16) Ogata, H.; Hirota, S.; Kamori, H.; Shibata, N.; Kato, T.; Kano, K.; Higuchi, Y. *Structure* **2005**, *13*, 1635–1642.
- (17) Brecht, M.; van Gastel, M.; Buhrke, T.; Friedrich, B.; Lubitz, W. *J. Am. Chem. Soc.* **2003**, *125*, 13075–13083.
- (18) Foerster, S.; van Gastel, M.; Brecht, M.; Lubitz, W. *J. Biol. Inorg. Chem.* **2005**, *10*, 51–62.
- (19) Fan, C.; Teixeira, M.; Moura, J. J. G.; Moura, I.; Huynh, B. H.; LeGall, J.; Peck, H. D., Jr.; Hoffman, B. M. *J. Am. Chem. Soc.* **1991**, *113*, 20–24.
- (20) Foerster, S.; Stein, M.; Brecht, M.; Ogata, H.; Higuchi, Y.; Lubitz, W. *J. Am. Chem. Soc.* **2003**, *125*, 83–93.
- (21) Foerster, S. Ph.D Thesis, Technische Universität Berlin, Germany, 2003.
- (22) Whitehead, J. P.; Gurbel, R. J.; Bagyinka, C.; Hoffman, B. M.; Maroney, M. J. *J. Am. Chem. Soc.* **1993**, *115*, 5629–5635.
- (23) van der Zwaan, J. W.; Coremans, J. M. C. C.; Bouwens, E. C. M.; Albracht, S. P. J. *Biochim. Biophys. Acta* **1990**, *1041*, 101–110.
- (24) Asso, M.; Guigliarelli, B.; Yagi, T.; Bertrand, P. *Biochim. Biophys. Acta* **1991**, *1122*, 50–56.
- (25) Brecht, M.; van Gastel, M.; Buhrke, T.; Friedrich, B.; Lubitz, W. *J. Am. Chem. Soc.* **2003**, *125*, 13075–13083.
- (26) Gessner, C.; Trofanchuk, O.; Kawagoe, K.; Higuchi, Y.; Yasuoka, N.; Lubitz, W. *Chem. Phys. Lett.* **1996**, *256*, 518–524.
- (27) Pavlov, M.; Siegbahn, P. E. M.; Blomberg, M. R. A.; Crabtree, R. H. *J. Am. Chem. Soc.* **1998**, *120*, 548–555.
- (28) Stadler, C.; De Lacey, A. L.; Montet, Y.; Volbeda, A.; Fontecilla-Camps, J. C.; Conesa, J. C.; Fernandez, V. M. *Inorg. Chem.* **2002**, *41*, 4424–4434.
- (29) Amara, P.; Volbeda, A.; Fontecilla-Camps, J. C.; Field, M. J. *J. Am. Chem. Soc.* **1999**, *121*, 4468–4477.
- (30) Stein, M.; Lubitz, W. *Phys. Chem. Chem. Phys.* **2001**, *3*, 2668–2675.
- (31) Stein, M.; van Lenthe, E.; Baerends, E. J.; Lubitz, W. *J. Am. Chem. Soc.* **2001**, *123*, 5839–5840.
- (32) Stein, M.; Lubitz, W. *Phys. Chem. Chem. Phys.* **2001**, *3*, 5115–5120.
- (33) Stein, M.; Lubitz, W. *J. Inorg. Biochem.* **2004**, *98*, 862–877.
- (34) Wu, L. F.; Mandrand, M. A. *FEMS Microbiol. Rev.* **1993**, *104*, 243–270.
- (35) Volbeda, A.; Fontecilla-Camps, J. C. *Dalton Trans.* **2003**, *21*, 4030–4038.
- (36) Chapman, A.; Cammack, R.; Hatchikian, E. C.; McCracken, J.; Peisach, J. *FEBS Lett.* **1988**, *242*, 134–138.
- (37) Buhrke, T.; Brecht, M.; Lubitz, W.; Friedrich, B. *J. Biol. Inorg. Chem.* **2002**, *7*, 897–908.
- (38) Jiang, F.; McCracken, J.; Peisach, J. *J. Am. Chem. Soc.* **1990**, *112*, 9035–9044.
- (39) Hunt, M. J.; MacKay, A. L.; Edmonds, D. T. *Chem. Phys. Lett.* **1975**, *34*, 473–475.
- (40) Palmer, M. H.; Scott, F. E.; Smith, J. A. S. *Chem. Phys.* **1983**, *74*, 9–14.
- (41) Rabbani, S. R.; Edmonds, D. T.; Gosling, P. J. *Magn. Reson.* **1987**, *72*, 230–237.
- (42) Palmer, M. H. *Z. Naturforsch., A: Phys. Sci.* **1984**, *39*, 1108–1111.
- (43) Ohmura, T.; Akutsu, H.; Nakamura, T. *Biosci. Biotech. Biochem.* **1996**, *60*, 2052–2054.
- (44) Lowry, O. H.; Rosenbrough, N. J.; Farr, A. L.; Randall, R. J. *J. Biol. Chem.* **1951**, *193*, 265–275.
- (45) van Gastel, M.; Coremans, J. W. A.; Jeuken, L. J. C.; Canters, G. W.; Groenen, E. J. *J. Phys. Chem. A* **1998**, *102*, 4462–4470.
- (46) The cancellation condition can be written in a less stringent way as $|v_n - |A|/2| < K$.⁴⁷
- (47) Flanagan, H. L.; Singel, D. J. *J. Chem. Phys.* **1987**, *87*, 5606–5616.
- (48) Mims, W. B.; Peisach, J. *J. Chem. Phys.* **1978**, *69*, 4921–4930.
- (49) Schweiger, A.; Jeschke, G. *Principles of Pulse Electron Paramagnetic Resonance*; Oxford University Press: Oxford, U. K., 2001.
- (50) Neese, F. *ORCA — An ab initio, Density Functional and Semiempirical Program Package*, version 2.4, revision 25; Max Planck Institut für Bioanorganische Chemie: Mülheim an der Ruhr, 2004.
- (51) Davidson, G.; Choudhury, S. B.; Gu, Z.; Bose, K.; Roseboom, W.; Albracht, S. P. J.; Maroney, M. J. *Biochemistry* **2000**, *39*, 7468–7479.
- (52) Ryde, U.; Olsson, M. H. M.; Pierloot, K.; Roos, B. O. *J. Mol. Biol.* **1996**, *261*, 586–596.
- (53) Neese, F. *J. Chem. Phys.* **2001**, *115*, 11080–11096.
- (54) Neese, F. *J. Chem. Phys.* **2003**, *118*, 3939–3948.
- (55) Trofanchuk, O.; Stein, M.; Gessner, C.; Lendzian, F.; Higuchi, Y.; Lubitz, W. *J. Biol. Inorg. Chem.* **2000**, *5*, 36–44.
- (56) Cammack, R.; Patil, D. S.; Aguirre, R.; Hatchikian, E. C. *FEBS Lett.* **1982**, *142*, 289–292.
- (57) Gessner, C.; Stein, M.; Albracht, S. P. J.; Lubitz, W. *J. Biol. Inorg. Chem.* **1999**, *4*, 379–389.
- (58) Garcia, M. L. S.; Smith, J. A. S.; Bavin, P. M. G.; Ganellin, C. R. *J. Chem. Soc., Perkin Trans. 2* **1983**, 1391–1399.
- (59) Ogata, H.; Hirota, S.; Nakahara, A.; Komori, H.; Shibata, N.; Kato, T.; Kano, K.; Higuchi, Y. *Structure* **2005**, *13*, 1635–1642.
- (60) Volbeda, A.; Charon, M.-H.; Hatchikian, E. C.; Frey, M.; Fontecilla-Camps, J. C. *Nature* **1995**, *373*, 580–587.
- (61) Manas, E. S.; Vanderkooi, J. M.; Sharp, K. A. *J. Phys. Chem. B* **1999**, *103*, 6334–6348.
- (62) Steiner, T. *Angew. Chem., Intl. Ed.* **2002**, *41*, 48–76.
- (63) Jeffrey, G. A. *An Introduction to Hydrogen Bonding*; Oxford University Press: Oxford, U. K., 1997.
- (64) Kleihues, L.; Lenz, O.; Bernhard, M.; Buhrke, T.; Friedrich, B. *J. Bacteriol.* **2000**, *182*, 2716–2724.